Biomaterials Science

ROYAL SOCIETY OF CHEMISTRY

PAPER

View Article Online
View Journal

Cite this: DOI: 10.1039/d4bm01155d

CaGA nanozymes with multienzyme activity realize multifunctional repair of acute wounds by alleviating oxidative stress and inhibiting cell apoptosis†

Zenghong Chen,‡[a] Xinyu Zhao,‡[b] Liting Lin,‡[c] Yuyu Cui,[a] Dongsheng Cao,*[a] Xu-Lin Chen*[b] and Xianwen Wang *[a,c]

Received 1st September 2024,
Accepted 26th September 2024

DOI: 10.1039/d4bm01155d

rsc.li/biomaterials-science

Acute wounds result from damage to the skin barrier, exposing underlying tissues and increasing susceptibility to bacterial and other pathogen infections. Improper wound care increases the risk of exposure and infection, often leading to chronic nonhealing wounds, which cause significant patient suffering. Early wound repair can effectively prevent the development of chronic nonhealing wounds. In this study, Ca-Gallic Acid (CaGA) nanozymes with multienzyme catalytic activity were constructed for treating acute wounds by coordinating Ca ions with gallic acid. CaGA nanozymes exhibit high superoxide dismutase/catalase (SOD/CAT) catalytic activity and good antioxidant performance *in vitro*. *In vitro* experiments demonstrated that CaGA nanozymes can effectively promote cell migration, efficiently scavenge ROS, maintain mitochondrial homeostasis, reduce inflammation, and decrease cell apoptosis. *In vivo*, CaGA nanozymes promoted granulation tissue formation, accelerated collagen fiber deposition, and reconstructed skin appendages, thereby accelerating acute wound healing. CaGA nanozymes have potential clinical application value in wound healing treatment.

1. Introduction

Currently, wound repair remains a critical social and medical issue.[1] The occurrence of acute wounds is often associated with trauma or surgery. The inflammatory response is a part of the wound healing process, but excessive inflammation can worsen tissue damage,[2,3] resulting in poor wound healing and ultimately the formation of chronic wounds.[4] Chronic wound formation is associated with multiple factors, such as wound size, depth, and infection. Owing to compromised skin barrier function, acute wounds expose the underlying tissues, making them prone to infections by bacteria and other pathogens.[5–7] Improper wound care increases the risk of exposure and infection, which often progresses to chronic nonhealing wounds, causing great suffering to patients. Early wound repair can effectively prevent wounds from progressing to a chronic nonhealing state. Today, various new biomaterials and regenerative medicine technologies continue to be developed to provide multiple options for tissue repair,[8,9] but how to effectively and safely apply these technologies to the clinical treatment of acute wounds remains a challenge.

Reactive oxygen species (ROS) are normal metabolic products of redox reactions within cells and are produced primarily by mitochondrial oxidation.[10,11] However, excessive ROS can trigger a series of harmful reactions, including apoptosis and inflammation. When skin tissue is damaged, ROS activate pathways such as the NF-κB pathway, leading to inflammation and promoting the secretion of inflammatory factors.[12–14] Gallic acid (GA) is a natural polyphenol with various biological activities, including anti-inflammatory,[15,16] antibacterial,[17,18] and antitumor[19,20] properties. The molecular structure of GA contains phenolic hydroxyl and carboxyl groups,[21,22] resulting in both polyphenol and carboxylic acid properties, making it prone to oxidation. Therefore, GAs are often used in industrial preservation and antiseptic applications. GA can scavenge various free radicals,[23] including nitrogen radicals, hydroxyl radicals, and superoxide anions. Additionally, GA and its

[a]Department of Plastic and Reconstructive Surgery, The Second Affiliated Hospital of Anhui Medical University, Hefei 230601, P. R. China.
E-mail: caodongsheng2017@163.com, xianwenwang@ahmu.edu.cn
[b]Department of Burns, The First Affiliated Hospital of Anhui Medical University, Hefei 230032, P. R. China. E-mail: okcxl@126.com
[c]School of Biomedical Engineering, Research and Engineering Center of Biomedical Materials, Anhui Provincial Institute of Translational Medicine, Anhui Medical University, Hefei, 230032, P. R. China

†Electronic supplementary information (ESI) available. See DOI: https://doi.org/10.1039/d4bm01155d

‡These authors contributed equally to this work.

derivatives also exhibit excellent enzyme-like activity.[24] GA can reduce intracellular oxidative stress levels, inhibit the production of intracellular ROS, and protect cells from oxidative stress damage.[25,26] GA also inhibits the release of inflammation-related factors, exerting anti-inflammatory effects.[15,27] However, the poor stability of GA in alkaline or neutral environments and its limited solubility in water restrict its biological activity. Calcium ions (Ca^{2+}) play crucial roles in cell signal transduction and physiological functions.[28,29] By regulating calcium-dependent signaling pathways, the production of proinflammatory cytokines can be reduced. Additionally, calcium ions can regulate mitochondrial homeostasis and change mitochondrial function, thus affecting the occurrence of oxidative stress.[30,31] During tissue repair, calcium ions promote wound healing by enhancing fibroblast migration.[32] Calcium ions can regulate processes such as cytoskeletal remodeling, focal adhesion formation, and disassembly through the formation of localized calcium signals, directly affecting cell migration ability. Moreover, calcium ions influence cell movement by modulating the polymerization and depolymerization of actin through calcium-binding proteins such as calmodulin,[33,34] thereby altering the dynamic structure of the cytoskeleton. Calcium ions also activate PKC, regulating migration-related signaling pathways and affecting cell polarity and directionality.[35,36]

Metal polyphenol coordination can organically integrate the properties of the two, and even show new properties.[37] To develop nanomaterials with multifunctional repair capabilities, this study successfully prepared CaGA nanozymes by coordinating calcium ions with gallic acid through alkalization. The constructed CaGA nanozymes exhibited high superoxide dismutase/catalase (SOD/CAT) catalytic activity and excellent *in vitro* antioxidant capacity. Cell experiments revealed that CaGA nanozymes promoted cell migration. Additionally, CaGA nanozymes are able to scavenge ROS generated by oxidative stress within cells, suppress intracellular inflammation, and maintain cell viability. Further experiments revealed that CaGA nanozymes could stabilize mitochondrial structures, reduce mitochondrial damage, and thereby decrease cell apoptosis. Animal experiments indicated that CaGA nanozymes could rapidly promote granulation formation in acute wounds, reducing the wound healing time. Moreover, CaGA nanozymes exhibited good biocompatibility, suggesting a novel strategy for promoting acute wound healing (Scheme 1).

2. Materials and methods

2.1 Materials

The Total SOD Assay Kit with WST-8 (Beyotime), H_2O_2 Assay Kit (Nanjing Jiancheng Bioengineering Institute, China), 1,1-diphenyl-2-picrylhydrazyl (DPPH), 2,2′-azino-bis(3-ethylbenzothiazoline-6-sulfonic acid) (ABTS) purchased from Macklin (Shanghai, China), CCK-8 Assay Kit (Spark Jade), Cell Apoptosis Kit (Bestbio), Cell Live/Dead Assay Kit (Bestbio), Mitochondrial Membrane Potential Assay Kit (Bestbio), and ROS Assay Kit (Beyotime) were used.

2.2 Preparation of CaGA nanozymes

Two mmol of gallic acid monohydrate was dissolved in a 0.05 M NaOH solution, added to a 10 mM $CaCl_2$ solution, and stirred for 1 hour. The mixture was subsequently adjusted to pH 7.0 and stirred continuously at room temperature. The solution obtained after 12 h of reaction was washed by centrifugation to obtain a brown precipitate, namely, CaGA nanozymes.

2.3 Characterization

The sample morphology was analyzed *via* transmission electron microscopy (JEM-1400 Plus, Japan). X-ray diffraction (XRD) patterns were measured *via* an X-ray diffractometer (DX-2700BH, Haoyuan, China) under 40 kV and 30 mA radiation. To determine the chemical composition of the sample (Thermo Scientific K-Alpha, China), X-ray photoelectron spectroscopy (XPS) was used. Fluorescence images were obtained *via* a laser confocal microscope (U-LH100HGAPO, Olympus Corporation). The UV-vis absorption spectrum of the substance was measured *via* a UV-vis spectrophotometer (Thermo Scientific Genesys 50, China). The optical density (OD) was measured *via* a multifunctional enzyme-linked immunosorbent assay (SpectraMax iD3, Shanghai).

2.4 Radical scavenging

Different concentrations of CaGA nanozymes were added to the prepared $ABTS^+$/DPPH radical working solutions.[38,39] After reacting in the dark, a UV-Vis spectrophotometer was used to measure the absorbance of the mixed solutions at 734/519 nm to assess the ability of the CaGA nanozymes to scavenge radicals.

2.5 Assessment of CAT-like activity

The H_2O_2 scavenging ability of the CaGA nanozymes was tested *via* an H_2O_2 assay kit. H_2O_2 reacts with ammonium molybdate to form a stable yellow complex, which presents an absorption peak at 405 nm. CaGA nanozymes at different concentrations were incubated with 2 mM H_2O_2 at 37 °C for 2 hours. After the reaction, the concentration of residual H_2O_2 was measured according to the manufacturer's instructions, and the H_2O_2 decomposition ability was calculated.

2.6 Assessment of SOD-like activity

Exploration of the superoxide anion ($O_2^{\bullet-}$)-scavenging activity of CaGA nanozymes. A SOD assay kit was used to evaluate $O_2^{\bullet-}$ scavenging activity according to the manufacturer's instructions. Different concentrations of CaGA nanozymes were added to the working solution. After standing for 10 min, the absorbance at 550 nm was measured *via* a microplate reader.

2.7 Cell migration experiment

L929 cells were uniformly seeded in 6-well plates, and scratches of the same width were made in each well. Different

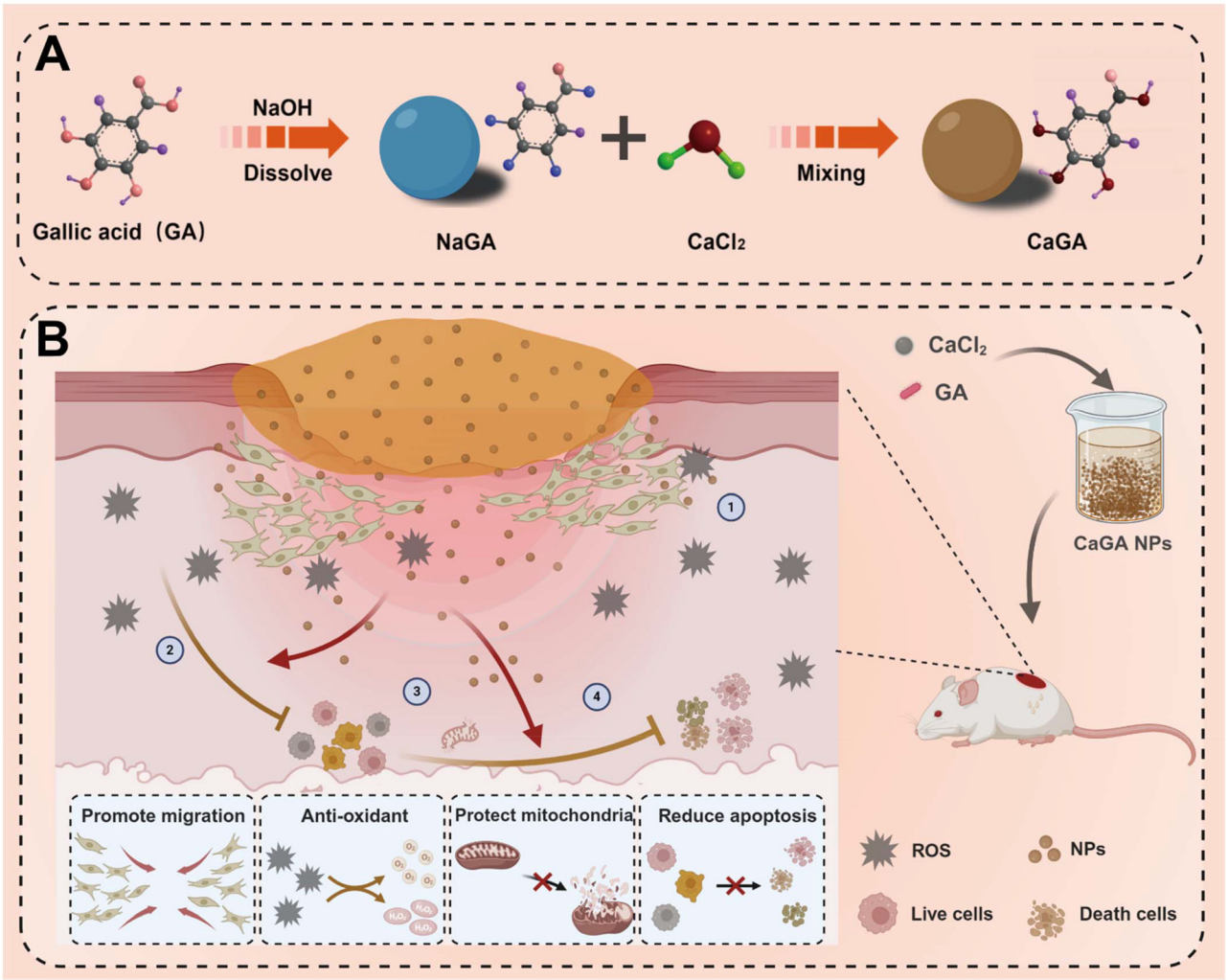

Scheme 1 (A) Schematic of the synthesis of CaGA nanozymes. (B) Schematic diagram of the treatment of acute wounds.

concentrations of CaGA nanozymes (0, 15, and 30 μg mL^{-1}) were added to each well. The degree of cell migration in each well was recorded at 0, 24, and 48 h.

2.8 Cell oxidative stress model

HUVECs were treated with a 1 mM H_2O_2 solution to establish an oxidative stress model. The samples were divided into a negative control group (Control), a model group (H_2O_2), a 15 μg mL^{-1} CaGA NP group (Low), and a 30 μg mL^{-1} CaGA NP group (High). Flow cytometry and fluorescence staining were performed according to the instructions of the ROS, cell apoptosis, live/dead, and mitochondrial membrane potential assay kits.

2.9 Transcriptome sequencing

The cell oxidative stress model was established *via* the aforementioned methods, and the cells were divided into H_2O_2 and CaGA NP groups. Transcriptomic sequencing was performed on the cells from both experimental groups. Differential gene analysis and statistics were conducted on the sequencing results, and enrichment analysis of the differentially expressed genes (DEGs) was performed.

2.10 Acute wound model

All animal procedures were performed in accordance with the Guidelines for Care and Use of Laboratory Animals of Anhui Medical University and approved by the Animal Ethics Committee of Anhui Medical University (no. LLSC20220731). The mice were randomly divided into the following 3 groups (n = 5): the PBS group, the GA group, and the CaGA NP group. First, the backs of all the mice were shaved, and the mice were anesthetized with sodium pentobarbital (40 mg kg^{-1}). A circular wound approximately 9 mm in diameter was made on the back skin. Immediately proceed with treatment after successful modeling. On days 0, 2, 4, 6, and 8 of treatment, photographs of the wounds were taken *via* a digital camera. The wound area was analyzed *via* ImageJ software, and the wound

healing rate was calculated. The calculation formula was as follows:

$$\text{Wound healing rate}\,(\%) = [\text{remaining wound area}/\text{original wound area}] \times 100.$$

2.11 Tissue section staining and hematological assessment

All the mice were euthanized after 8 days of treatment. Important organs were stained with hematoxylin–eosin (H&E). Skin tissues were analyzed histologically *via* H&E and Masson's trichrome staining. Images were collected *via* a slide scanner. Additionally, blood from each group was collected for serum biochemical assays (liver and kidney function markers), and complete blood counts were performed to evaluate the *in vivo* biocompatibility of the CaGA nanozymes.

2.12 Statistical analysis

Statistical analysis was performed on the data from each experimental group. The numerical data are expressed as the mean ± standard deviation ($X \pm SD$). The number of statistical cases in each group is greater than or equal to 3. Student's t test was used to compare the data between groups to determine whether there were significant differences. A significance level of $P < 0.05$ indicated statistical significance ($^{*}p < 0.05$, $^{**}p < 0.01$, $^{***}p < 0.005$, and $^{****}p < 0.001$).

3. Results and discussion

3.1 Characterization of CaGA nanozymes

CaGA nanozymes are formed by coordinating calcium chloride nanozymes with the natural product gallic acid (Fig. 1A). Transmission electron microscopy (TEM) images (Fig. 1B) revealed that the synthesized CaGA nanozymes had a uniform morphology, a low degree of agglomeration, and a particle size of approximately 200–300 nm (Fig. 1C). Owing to the presence of negatively charged –OH and –COOH groups on the surface of gallic acid, its zeta potential is negative. However, after coordinating with metal ions to form complexes, the zeta potential (Fig. 1D) remains negative, and the nanozymes as a whole present a negative charge. This approach has a wide range of applications in biochemistry and lays the foundation for further experiments. Afterward, the FTIR (Fig. 1E) spectra showed characteristic bands. After coordination with metal ions, the stretching vibrations of the 3200–3400 cm^{-1} phenolic group and 1660.30 cm^{-1} carboxyl group (indicated by arrows) disappeared, indicating that the H of GA was replaced by the metal ion Ca. The XRD results indicate that the CaGA nanozymes are amorphous (Fig. S1†). The XPS spectrum of the CaGA nanozymes shows two peaks at 347.40 eV and 350.93 eV (Fig. 1F and G). These results indicate that the oxidation state of Ca in CaGA is +2. The XPS peaks for C and O at 284.8 eV and 531.39 eV correspond to the +4 oxidation state of C and the −2 oxidation state of O, respectively (Fig. S2 and S3†). These findings confirmed the successful synthesis of the CaGA nanozymes. In conclusion, this study successfully synthesized novel nanozymes with a uniform morphology, and characterization methods such as FTIR, XRD, and XPS confirmed the coordination between Ca and GA. This provides a new approach for the synthesis and development of nanomaterials.

3.2 Multienzyme-like antioxidative activity of CaGA nanozymes

The resolution of inflammation plays a crucial role in regulating the healing process of wounds. Inflammation is often accompanied by the production of a large amount of ROS, leading to oxidative stress, which is a key factor hindering wound healing. Fig. 2A shows the anti-inflammatory activity of the CaGA nanozymes. $ABTS^{+}$ and DPPH were used to determine the ability of $ABTS^{+}$ and DPPH to remove ROS and reactive nitrogen. In the $ABTS^{+}$ probe experiment, CaGA nanozymes at a concentration of 20 μg mL^{-1} were able to scavenge 78% of the free radicals, and the color of the solution gradually decreased from blue (Fig. 2B and E). In the DPPH probe experiment, more than 90% of the free radicals were cleared by the 20 μg mL^{-1} CaGA nanozymes, and the solution gradually changed from purple to light purple (Fig. 2C and F). Under physiological conditions, SOD acts as the main antioxidant enzyme, catalyzing superoxide anion ($O_2^{\bullet-}$) into O_2 and H_2O_2,[40,41] which are then converted into nontoxic H_2O and O_2 by CAT.[42–44] Therefore, the cascade catalytic activity of SOD and CAT can protect organisms from excessive ROS damage.[45,46] The SOD-like and CAT-like activities of the CaGA nanozymes were studied below. The SOD-like enzyme activity of CaGA nanozymes was explored *via* the WST-8 method. When the concentration of CaGA nanozymes was 150 μg mL^{-1}, the inhibition rate of $O_2^{\bullet-}$ was 98%, indicating that CaGA nanozymes have the ability to clear superoxide anions (Fig. 2D). The experiments revealed that CaGA nanozymes can catalyze H_2O_2 to produce oxygen, exert effects on CAT-like enzymes, and exhibit concentration-dependent activity. Approximately 99% of H_2O_2 is decomposed by 100 μg mL^{-1} CaGA nanozymes (Fig. 2G). The above experiments confirmed that CaGA nanozymes exhibit good SOD/CAT enzyme activity and strong antioxidant capabilities *in vitro*, providing a theoretical basis for subsequent cell and animal experiments.

3.3 CaGA nanozymes promote cell migration

Before the cell experiments were started, the biocompatibility of the material with cells was investigated. The results (Fig. S4†) revealed that when the concentration of the CaGA nanozymes reached 200 μg mL^{-1}, the viability of the HUVECs remained as high as 100%. Cell migration is a crucial step in wound healing,[47,48] where fibroblasts and epithelial cells migrate from surrounding tissues to the wound site, contributing to granulation tissue and new skin formation. This study investigated the effects of different concentrations of CaGA nanozymes on cell migration. Microscopy images of cell migration (Fig. 3A) revealed that after 24 hours, the cells in the control group exhibited minimal migration. In contrast, the cells in the other two groups exhibited varying degrees of migration, which was positively correlated with the material

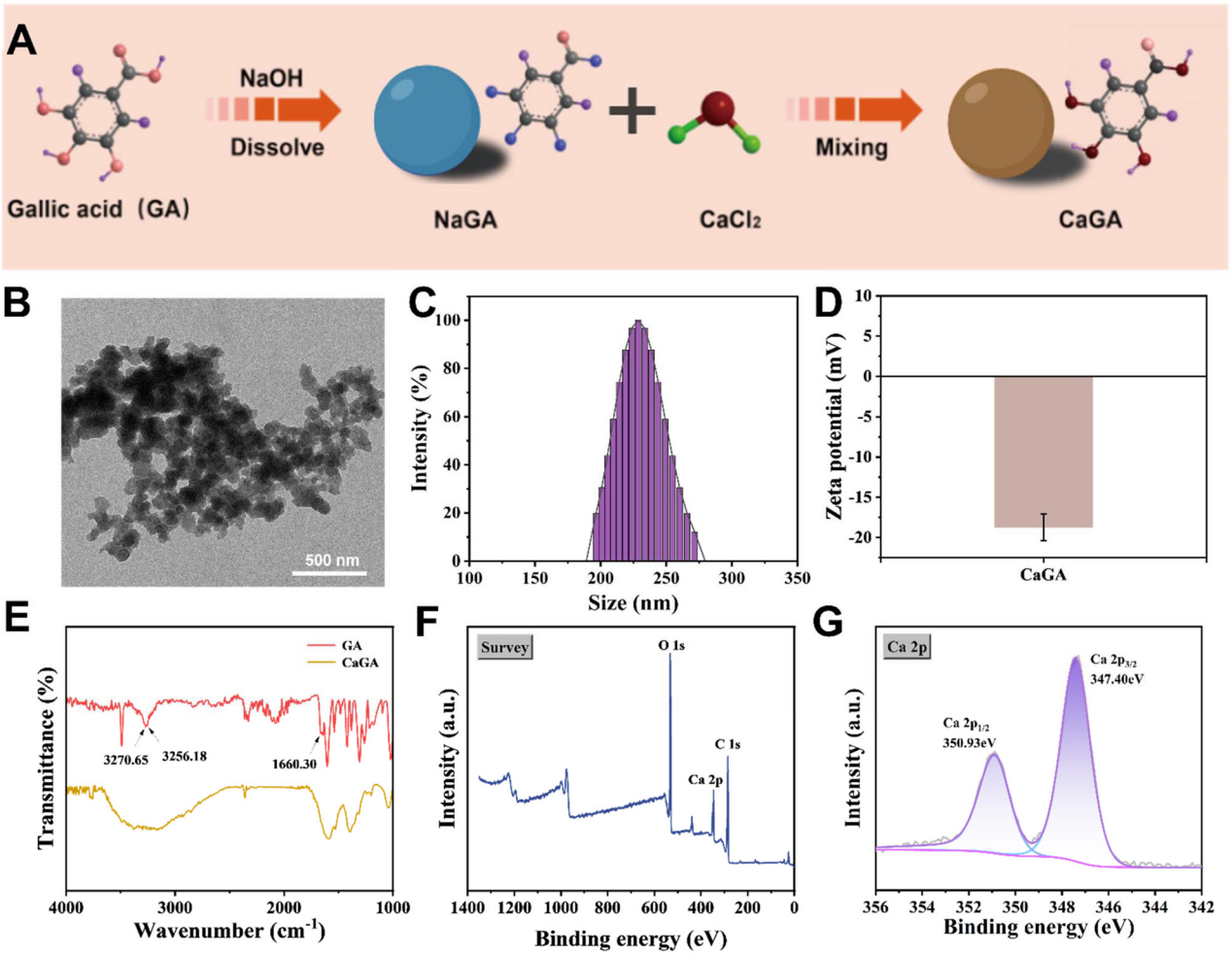

Fig. 1 Preparation and characterization of CaGA nanozymes. (A) Schematic of the synthesis of CaGA nanozymes. (B) TEM images of CaGA nanozymes. (C) Particle size distribution of CaGA nanozymes. (D) Zeta potential of CaGA nanozymes (n = 3). (E) FTIR spectra of CaGA nanozymes. (F) Full-spectrum XPS spectrum of CaGA nanozymes. (G) XPS spectrum of the Ca 2p orbital.

concentration. After 48 h, the migration rate of the control group of cells was only 8.53%, the low-concentration material group had a migration rate of 42.79%, and the high-concentration material group had a migration rate of up to 80.07% (Fig. 3B). These results indicated that CaGA nanozymes effectively promoted cell migration and that the extent of migration was positively correlated with the material concentration. This may be because the Ca in CaGA nanozymes can directly participate in the conduction of calcium signals and further regulate the activity of calcium-dependent proteins, thereby affecting the migration behavior of cells.

3.4 CaGA nanozymes reduce oxidative stress, alleviate inflammation, and decrease cell apoptosis

Next, this research investigated the ability of CaGA nanozymes to protect cells from oxidative stress damage. The results revealed that cells treated with H_2O_2 exhibited significant oxidative stress, with prominent green fluorescence after ROS staining (Fig. 3C). In contrast, the groups treated with CaGA nanozymes presented a significant reduction in ROS-associated green fluorescence. Moreover, the clearance of ROS by these materials also exhibited a concentration-dependent effect. Flow cytometry for ROS detection (Fig. 3D) indicated that CaGA NP treatment resulted in a cell population predominantly in the low-ROS region, confirming these findings. When cell viability and death were assessed, H_2O_2-induced cells presented a marked increase in cell death, as evidenced by increased red fluorescence and decreased green fluorescence (Fig. 3F). The low-concentration treatment also induced a degree of cell death, whereas the high-concentration treatment resulted in a lower cell death rate. These results suggest that CaGA NP treatment effectively reduces H_2O_2-induced cell death. The mitochondrial membrane potential is a crucial indicator of mitochondrial function, with a high membrane potential correlated with increased red fluorescence and a low membrane potential with increased green fluorescence. H_2O_2 induction led to a decreased mitochondrial membrane potential (Fig. 3E), and with increasing concen-

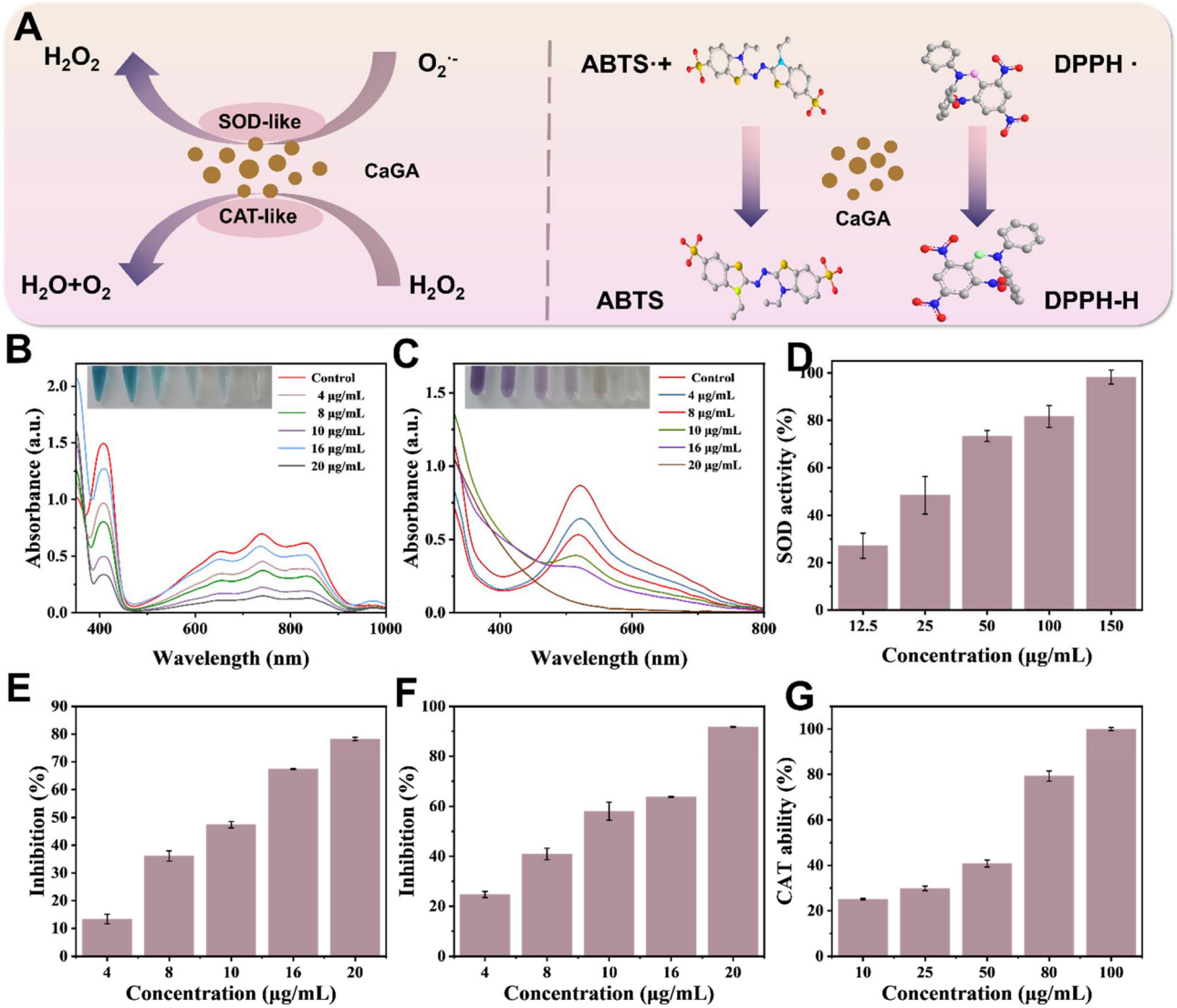

Fig. 2 *In vitro* free radical scavenging capacity and enzyme-like activity of CaGA nanozymes. (A) Schematic diagram of the free radical scavenging and enzyme-like activities of CaGA nanozymes. (B and C) UV absorbance curves of scavenged $ABTS^+$ radicals and DPPH radicals. (D) SOD-like enzyme activity (n = 3). (E and F) Rates of $ABTS^+$ and DPPH radical scavenging by CaGA nanozymes (n = 3). (G) CAT-like enzyme activity (n = 3).

trations of CaGA nanozymes, green fluorescence was gradually replaced by red fluorescence, indicating the protective effect of CaGA nanozymes on mitochondria. Changes in the mitochondrial membrane potential are often early markers of apoptosis. Flow cytometry was used to assess the apoptotic status of H_2O_2-induced cells (Fig. 3G). The results revealed that the control group had a high survival rate (88.1%) and low apoptosis rate (10.74%), whereas the H_2O_2 treatment group had a significantly increased apoptosis rate (89.8%), particularly late apoptosis (61.7%). Both the low-concentration (89.8% *vs.* 14.65%) and high-concentration (89.8% *vs.* 12.07%) treatment groups exhibited some degree of cell apoptosis, with most cells remaining viable. The above results demonstrate that CaGA nanozymes have strong ROS scavenging abilities in the face of oxidative stress, protecting mitochondrial function, maintaining cell viability, and reducing apoptosis.

3.5 Mechanistic exploration of CaGA nanozymes against oxidative stress

To further understand the mechanism by which CaGA nanozymes protect cells from oxidative stress damage, transcriptomic sequencing was performed on both the H_2O_2 group and the CaGA NP-treated group. The H_2O_2 group was used as the control for DEG analysis. The heatmap shows the differential gene expression between the two groups (Fig. 4A). In comparison, the CaGA NP-treated group had 2857 genes whose expression was upregulated, 1625 genes whose expression was downregulated, and 12 128 genes whose expression was not significantly different (Fig. 4B). KEGG enrichment analysis revealed significant enrichment of pathways related to inflammation and apoptosis (Fig. 4C). Further enrichment analysis of the DEGs, shown in the circular bar plots (Fig. 4D–G),

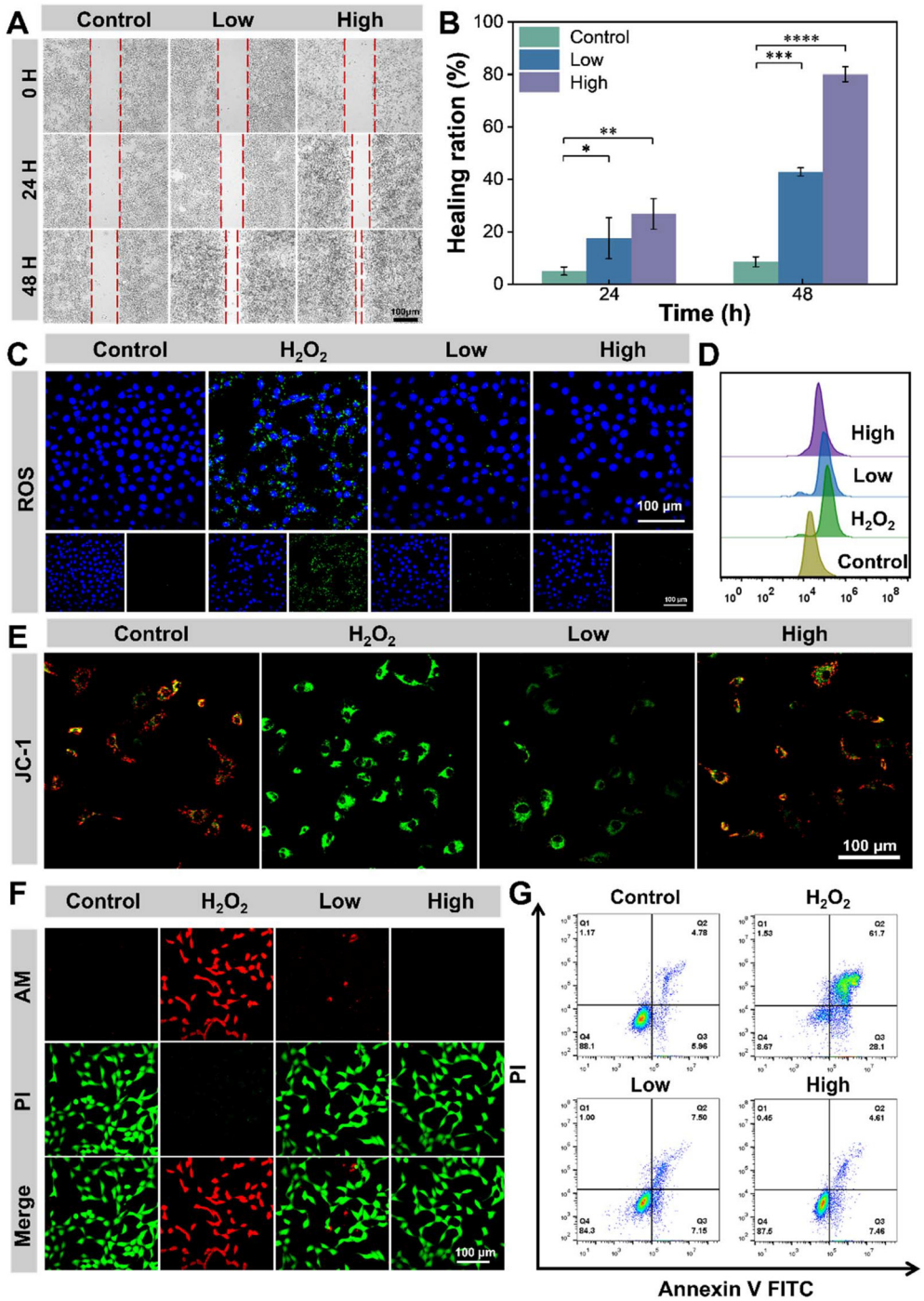

Fig. 3 CaGA nanozymes promote cell migration and protection against cell damage. (A) Microscopy images of the promotion of L929 cell migration. (B) Statistical analysis of the cell migration rate (n = 3). (C) Confocal fluorescence images of ROS. (D) Flow cytometry detection of ROS levels. (E and F) Confocal fluorescence images of living/dead JC-1 cells. (G) The extent of cell apoptosis was detected by flow cytometry.

revealed gene expression in the NF-κB, TNF, apoptosis, and P53 signaling pathways. Additionally, protein interaction network analysis (Fig. 4H) revealed the interaction network among proteins related to inflammation and apoptosis. The sequencing results indicate that CaGA nanozymes downregulate the NF-κB and TNF-α inflammatory pathways, reducing inflammation levels. Furthermore, CaGA nanozymes effectively downregulate the apoptosis and P53 signaling pathways, inhibiting cell apoptosis. After treatment with CaGA, several genes related to mitochondrial function, including Bcl-2, cytochrome-*c*, XIAP, and caspase-3, were significantly downregulated. These key genes play important roles in protecting cells from oxidative stress damage, reducing inflammation, and inhibiting apoptosis.

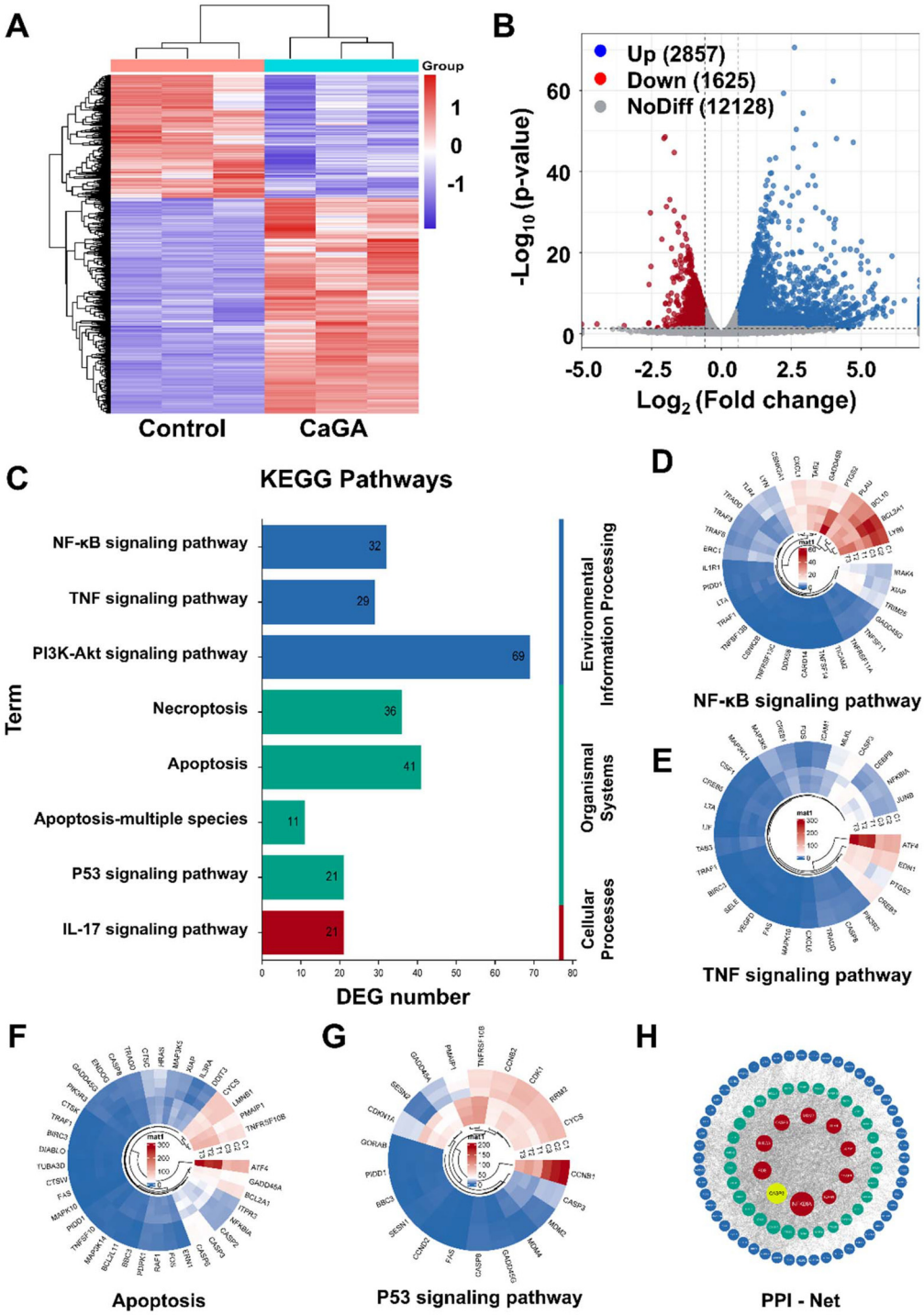

Fig. 4 The mechanism by which CaGA nanozymes alleviate oxidative stress injury. (A) Heatmap of significantly up- and downregulated genes. (B) Volcano plots of up- and downregulated genes. (C) KEGG enrichment analysis of the DEGs associated with inflammation and apoptosis. (D–G) Ring bar diagram of DEGs in the NF-κB, TNF, apoptosis, and P53 signaling pathways. (H) PPIs are associated with inflammation and apoptosis.

3.6 CaGA nanozymes promote wound healing *in vivo*

To study the effects of CaGA nanozymes on acute wound healing *in vivo*, a full-thickness skin injury model was established, and wounds treated with different interventions were recorded and subjected to relevant tissue staining (Fig. 5A). Compared with the PBS group, both the GA and CaGA NP groups promoted wound healing (Fig. 5B), with the CaGA NP group showing almost complete healing of the wound by day 8 of treatment. Statistical analysis of the wound healing rate

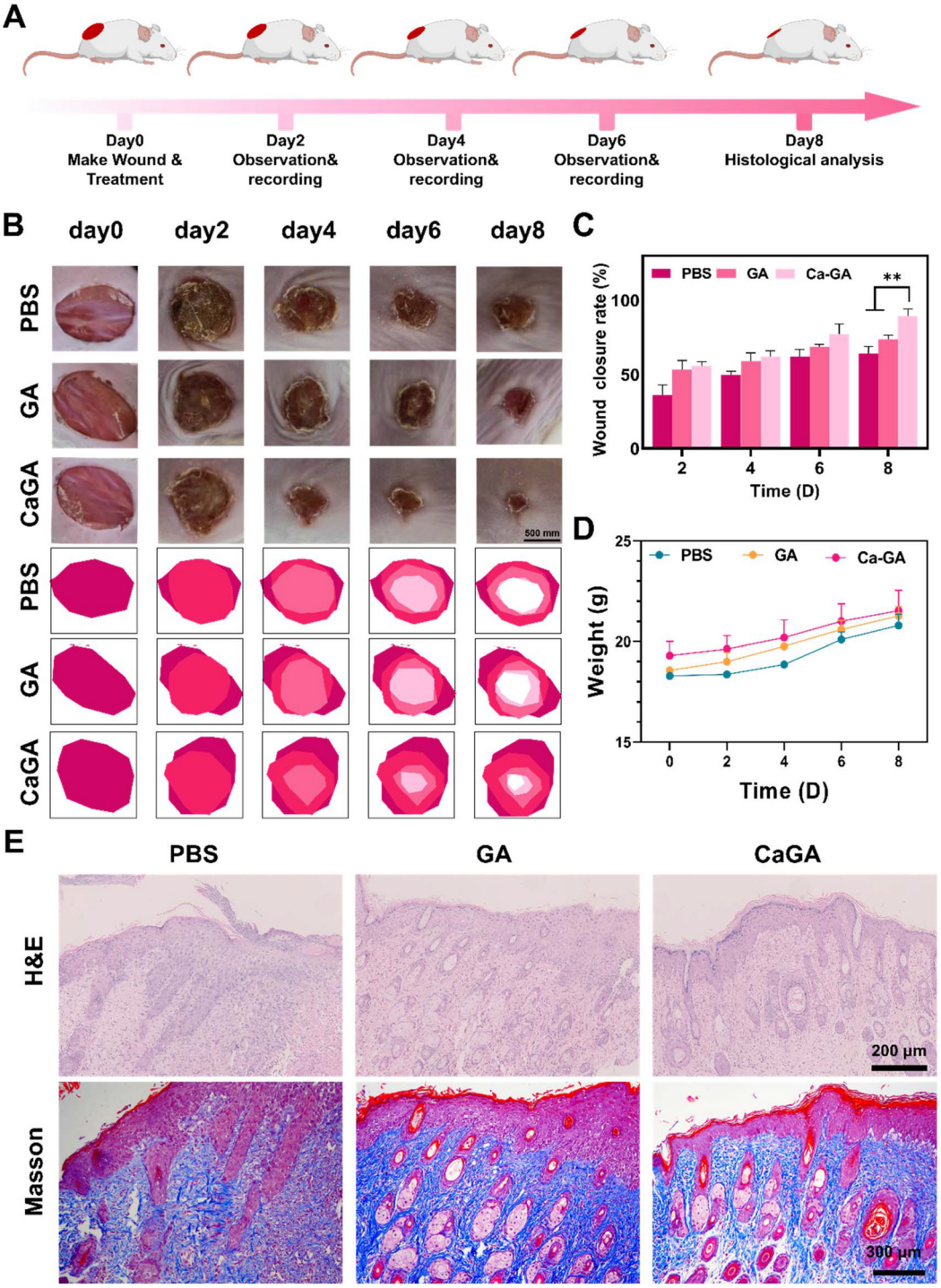

Fig. 5 CaGA NP treatment of acute wounds *in vitro*. (A) Treatment model diagram of acute wounds. (B) Photographs of wounds after different treatments. (C) Statistical analysis of the wound healing ratio (n = 3). (D) Weight changes in the mice (n = 3). (E) H&E and Masson staining of the wound on day 8.

(Fig. 5C) revealed that 89.34% of the mice in the CaGA NP group healed on day 8, whereas 63.82% and 73.37% of those in the control and GA groups, respectively, healed. To further validate the observed healing, histopathological analysis of the skin tissues was performed. Skin tissues from day 8 mice were stained with hematoxylin and eosin (H&E) and Masson's trichrome (Fig. 5E). H&E and Masson staining revealed greater granulation tissue and increased collagen fiber density in the CaGA-NP group than in the control group. The semiquantitative statistics of the slices revealed that the epithelial thickness

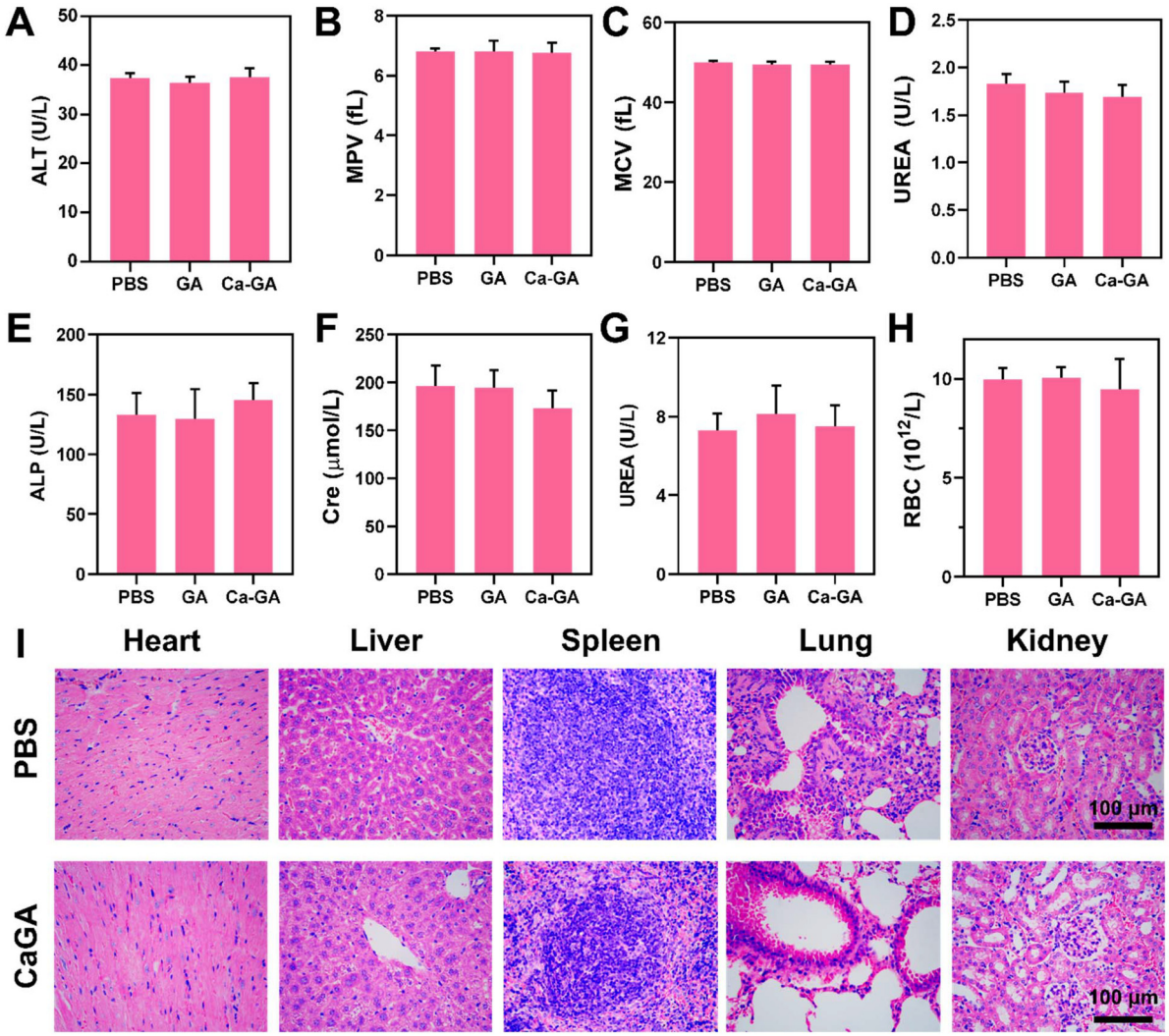

Fig. 6 Assessment of the biocompatibility of CaGA nanozymes. (A–H) Blood parameters and biochemical indices of mice in different groups on day 8 (n = 3). (I) Images of H&E-stained sections of major organs (heart, liver, spleen, lungs, and kidneys) from the different groups on day 8.

of the CaGA nanozyme-treated group was significantly reduced and that granulation tissue was increased (Fig. S5 and S6†). Additionally, new hair follicles were observed in the regenerated dermal tissue. These results indicate that CaGA nanozymes promote acute wound healing by increasing collagen deposition and granulation tissue formation. This study also monitored body weight changes in the mice during the experiment (Fig. 5D) and revealed a slight increase in body weight, with no significant differences among the three groups. The above results confirmed that CaGA nanozymes promote acute wound healing *in vivo* without significantly affecting the overall health of the animals.

3.7 *In vivo* biocompatibility assessment of CaGA nanozymes

On the 8th day of the acute wound treatment period, routine blood and biochemical tests were conducted on the mice from each treatment group (Fig. 6A–H). The results revealed that key parameters in the routine blood and biochemical tests of the mice treated with CaGA nanozymes were within normal ranges and did not significantly differ from those of the control group. Additionally, to comprehensively evaluate the *in vivo* biocompatibility of the CaGA nanozymes, histological analysis of major organs (heart, liver, spleen, lungs, and kidneys) was performed *via* H&E staining (Fig. 6I). The results indicated that the tissue structures of these organs were intact, with no significant morphological changes or inflammatory responses observed. These findings demonstrated that CaGA nanozymes exhibited good *in vivo* biocompatibility during the treatment of mouse wounds.

4. Conclusion

This study developed a metal-polyphenol nanozyme with multienzyme activity that exhibits excellent antioxidant properties *in vitro*. *In vitro* experiments demonstrated that CaGA nano-

zymes effectively promoted cell migration. Additionally, CaGA nanozymes efficiently scavenge H_2O_2-induced ROS, maintain mitochondrial homeostasis, and reduce inflammation, thereby decreasing cell apoptosis. The *in vivo* results indicate that CaGA nanozymes enhance granulation tissue formation, accelerate collagen deposition, and reconstruct skin appendages, thereby accelerating acute wound healing. Furthermore, the CaGA nanozymes showed good biocompatibility, providing solid safety assurance for the development and application of CaGA nanozymes. In summary, CaGA nanozymes have potential clinical application value in wound healing treatment.

Author contributions

Zenghong Chen: conceptualization, methodology, writing – original draft; Xinyu Zhao and Liting Lin: methodology, data curation; Yuyu Cui: methodology, data curation; Dongsheng Cao, Xu-Lin Chen and Xianwen Wang: funding acquisition, writing – review & editing, supervision. All the authors have read and agreed to the published version of the manuscript.

Data availability

All relevant data are within the manuscript and its additional files. The data are available from the corresponding author on reasonable request.

Conflicts of interest

The authors declare that they have no competing financial interests.

Acknowledgements

This work was supported by the National Natural Science Foundation of China (82172204, 82372552, 82372517), the Excellent Youth of Natural Science Research Projects in Anhui Province Universities (2023AH030060), the Anhui Key Research and Development Plan (Grant no. 202104j07020027), the Research Fund of Anhui Institute of Translational Medicine (2022zhyx-C01), the Natural Science Foundation of Anhui Medical University (2023xkj165), Scientific Research Foundation of the Education Department in Anhui Province (No. 2024AH050799), List of Municipal Key Common Technology R&D Projects in the Third Batch of Hefei City in 2022 (GJ2022SM02), and the Basic and Clinical Cooperative Research and Promotion Program of Anhui Medical University (2021xkT028). The authors would like to thank the Shiyan Laboratory (**https://www.shiyanjia.com**) for their help in language polishing. The Scheme 1 was created by **Biorender.com**.

References

1 A. C. de Oliveira Gonzalez, T. F. Costa, Z. de Araújo Andrade and A. R. A. P. Medrado, *An. Bras. Dermatol.*, 2016, **91**, 614–620.
2 P. Henson and R. B. Johnston, *J. Clin. Invest.*, 1987, **79**, 669–674.
3 C. Nathan, *Nature*, 2002, **420**, 846–852.
4 Z. Xu, B. Liang, J. Tian and J. Wu, *Biomater. Sci.*, 2021, **9**, 4388–4409.
5 D. Leaper, O. Assadian and C. E. Edmiston, *Br. J. Dermatol.*, 2015, **173**, 351–358.
6 J. Wang, X.-Y. Chen, Y. Zhao, Y. Yang, W. Wang, C. Wu, B. Yang, Z. Zhang, L. Zhang and Y. Liu, *ACS Nano*, 2019, **13**, 11686–11697.
7 W. Wang, Y. Cui, X. Wei, Y. Zang, X. Chen, L. Cheng and X. Wang, *ACS Nano*, 2024, **18**, 15845–15863.
8 S. J. Forbes and N. Rosenthal, *Nat. Med.*, 2014, **20**, 857–869.
9 L. Zhang and T. J. Webster, *Nano Today*, 2009, **4**, 66–80.
10 J. Liu, X. Han, T. Zhang, K. Tian, Z. Li and F. Luo, *J. Hematol. Oncol.*, 2023, **16**, 116.
11 C. Holze, C. Michaudel, C. Mackowiak, D. A. Haas, C. Benda, P. Hubel, F. L. Pennemann, D. Schnepf, J. Wettmarshausen and M. Braun, *Nat. Immunol.*, 2018, **19**, 130–140.
12 Q. Cheng, H. Geng, C. Zhang, X. Zhang, Y. Tian and J. Cui, *ACS Appl. Mater. Interfaces*, 2024, **16**, 48607–48618.
13 X. Cui, Z. Gao, K. Zhao, N. Wang, Q. Yu, M. Ashokkumar, J. Hao and J. Cui, *Chem. Mater.*, 2024, **36**, 8864–8871.
14 H. Geng, Z. Li, Z. Li, Y. Zhang, Z. Gao, L. Sun, X. Li, J. Cui, S. Ni and J. Hao, *Proc. Natl. Acad. Sci. U. S. A.*, 2023, **120**, e2220300120.
15 J. Bai, Y. Zhang, C. Tang, Y. Hou, X. Ai, X. Chen, Y. Zhang, X. Wang and X. Meng, *Biomed. Pharmacother.*, 2021, **133**, 110985.
16 Q. Li, C. Zhang, M. Zhu, J. Shan, H. Qian, Y. Ma and X. Wang, *Acta Biomater.*, 2024, **182**, 260–274.
17 A. Lunkov, B. Shagdarova, M. Konovalova, Y. Zhuikova, N. Drozd, A. Il'ina and V. Varlamov, *Carbohydr. Polym.*, 2020, **234**, 115916.
18 Y. Huang, Y. Chen, Z. Lu, B. Yu, L. Zou, X. Song, H. Han, Q. Jin and J. Ji, *Small*, 2023, **19**, 2302578.
19 C. Locatelli, F. B. Filippin-Monteiro and T. B. Creczynski-Pasa, *Eur. J. Med. Chem.*, 2013, **60**, 233–239.
20 C. Locatelli, F. B. Filippin-Monteiro, A. Centa and T. B. Creczinsky-Pasa, *Handbook on Gallic Acid: Natural Occurrences, Antioxidant Properties and Health Implications*, Nova Publishers, 4th edn, 2013, vol. 1, p. 23.
21 Q. Wang, K. Zhou, Y. Ning and G. Zhao, *Food Chem.*, 2016, **213**, 260–267.
22 J. Zhao, I. A. Khan and F. R. Fronczek, *Acta Crystallogr., Sect. E: Struct. Rep. Online*, 2011, **67**, o316–o317.
23 V. K. Rajan and K. Muraleedharan, *Food Chem.*, 2017, **220**, 93–99.
24 H. Tian, J. Yan, W. Zhang, H. Li, S. Jiang, H. Qian, X. Chen, X. Dai and X. Wang, *Acta Biomater.*, 2023, **167**, 449–462.

25 M. Senevirathne, Y.-J. Jeon, Y.-T. Kim, P.-J. Park, W.-K. Jung, C.-B. Ahn and J.-Y. Je, *Carbohydr. Polym.*, 2012, **87**, 876–880.
26 M. Marzano, N. Borbone, F. Amato, G. Oliviero, P. Fucile, T. Russo and F. Sannino, *Gels*, 2022, **8**, 124.
27 J. Zheng, T. Chen, K. Wang, C. Peng, M. Zhao, Q. Xie, B. Li, H. Lin, Z. Zhao and Z. Ji, *ACS Nano*, 2024, **18**, 2355–2369.
28 M. Kohlhaas and C. Maack, *Cardiovasc. Res.*, 2013, **98**, 259–268.
29 T. Finkel, S. Menazza, K. M. Holmström, R. J. Parks, J. Liu, J. Sun, J. Liu, X. Pan and E. Murphy, *Circ. Res.*, 2015, **116**, 1810–1819.
30 E. Bertero and C. Maack, *Circ. Res.*, 2018, **122**, 1460–1478.
31 G. S. Williams, L. Boyman, A. C. Chikando, R. J. Khairallah and W. Lederer, *Proc. Natl. Acad. Sci. U. S. A.*, 2013, **110**, 10479–10486.
32 C. Navarro-Requena, S. Pérez-Amodio, O. Castano and E. Engel, *Nanotechnology*, 2018, **29**, 395102.
33 T. Meyer, P. I. Hanson, L. Stryer and H. Schulman, *Science*, 1992, **256**, 1199–1202.
34 D. Chin and A. R. Means, *Trends Cell Biol.*, 2000, **10**, 322–328.
35 P. Costa, L. M. Blowes, A. C. Laly and J. T. Connelly, *Acta Biomater.*, 2021, **126**, 291–300.
36 C. Wei, X. Wang, M. Zheng and H. Cheng, *Curr. Opin. Cell Biol.*, 2012, **24**, 254–261.
37 H. Geng, Q.-Z. Zhong, J. Li, Z. Lin, J. Cui, F. Caruso and J. Hao, *Chem. Rev.*, 2022, **122**, 11432–11473.
38 Y. Jiang, X. Feng, X. Qiao, Y. Li, X. Li, J. Yang and L. Han, *Bioact. Mater.*, 2024, **41**, 523–536.
39 Y. Wu, X. Chen, Z. Zeng, B. Chen, Z. Wang, Z. Song and H. Xie, *Bioact. Mater.*, 2024, **39**, 595–611.
40 J. Li, J. Song, Z. Deng, J. Yang, X. Wang, B. Gao, Y. Zhu, M. Yang, D. Long and X. Luo, *Bioact. Mater.*, 2024, **36**, 203–220.
41 Z. Deng, W. Ma, C. Ding, C. Wei, B. Gao, Y. Zhu, Y. Zhang, F. Wu, M. Zhang and R. Li, *Nano Today*, 2023, **53**, 102044.
42 R. Zhang, L. Chen, Q. Liang, J. Xi, H. Zhao, Y. Jin, X. Gao, X. Yan, L. Gao and K. Fan, *Nano Today*, 2021, **41**, 101317.
43 R. Zhang, B. Xue, Y. Tao, H. Zhao, Z. Zhang, X. Wang, X. Zhou, B. Jiang, Z. Yang and X. Yan, *Adv. Mater.*, 2022, **34**, 2205324.
44 X. Du, B. Jia, W. Wang, C. Zhang, X. Liu, Y. Qu, M. Zhao, W. Li, Y. Yang and Y.-Q. Li, *J. Nanobiotechnol.*, 2022, **20**, 12.
45 Q. Li, M. Dong, Q. Han, Y. Zhang, D. Yang, D. Wei and Y. Yang, *J. Controlled Release*, 2024, **365**, 905–918.
46 X. Jin, W. Zhang, J. Shan, J. He, H. Qian, X. Chen and X. Wang, *ACS Appl. Mater. Interfaces*, 2022, **14**, 50677–50691.
47 W. S. Krawczyk, *J. Cell Biol.*, 1971, **49**, 247.
48 A. Tremel, A. Cai, N. Tirtaatmadja, B. D. Hughes, G. W. Stevens, K. A. Landman and A. J. O'Connor, *Chem. Eng. Sci.*, 2009, **64**, 247–253.

